Determining the lifetime of the first 4^+ state in ^{182}Pt

Sanna Stolze

Master's Thesis

University of Jyväskylä, Department of Physics
Supervisors: Professor R. Julin and Dr. T. Grahn
September 22, 2011

Abstract

In this work the mean lifetime of the first 4^+ state in ^{182}Pt was determined by using the Recoil Distance Doppler-Shift method. The studied nuclei were produced in the ^{86}Kr(^{100}Mo, 4n)^{182}Pt fusion-evaporation reaction. The RDDS method exploits the fact that the observed γ-ray energy depends on the velocity of the emitting nucleus. Using a degrader foil after the target enables measuring the intensities of γ-rays emitted before and after the degrader. The recoil-gated $\gamma\gamma$ spectra were analyzed separately for each target-to-degrader distance and the lifetime was determined with the Differential Decay Curve Method, which takes into account the lifetimes of the feeding states.

The lifetime of the 4^+ state in ^{182}Pt was determined to be $\tau = 40.8(14)$ ps. This corresponds to a transition quadrupole moment of $|Q_t| = 6.90(12)\,e$b. When comparing the quadrupole moment to other $N = 104$ isotones it is clear, even when taking into account the charge dependence of the quadrupole moment, that the quadrupole moment of the prolate 4^+ state in ^{186}Pb is significantly larger. Also the quadrupole moments decrease with decreasing Z. Before drawing any final conclusions about the collectivity of the prolate band in ^{182}Pt it is neccessary to determine the lifetimes of other yrast excited states at low energies.

Tiivistelmä

Tässä työssä määritettiin ^{182}Pt:n ensimmäisen 4^+-viritystilan elinaika. Tutkittavat ytimet tuotettiin ^{86}Kr(^{100}Mo, 4n)^{182}Pt fuusiohöyrystysreaktiolla. Elinaika määritettiin RDDS-memetelmällä (Recoil Distance Doppler-Shift method), jossa hyödynnetään havaitun gammasäteilyn energian riippuvuutta säteilyn emittoineen ytimen nopeudesta. Käyttämällä hidastinkalvoa kohtion takana voidaan havaitusta säteilystä määrittää, onko se emittoitu ennen hidastinkalvoa vai sen jälkeen.

Mittalaitteistoon kuului JUROGAM II -germaniumilmaisinasetelma kohtion ympärillä γ-säteiden havaitsemiseen ja plunger-laite, jolla kohtion ja hidastinkalvon etäisyyttä pystyyttiin muuttamaan ja mittaamaan tarkasti. Lisäksi käytettiin RITU-rekyyliseparaattoria ja sen fokaalitasolla sijaisevaa GREAT-spektrometriä erottamaan ja tunnistamaan fuusiohöyrysreaktioissa tuotetut rekyylit alkuperäisestä suihkusta, irronneista kohtion ioneista ja fissiotuotteista.

Rekyylivarmennetuista samanaikaisista γ-säteistä muiodostetut spektrit analysoitiin erikseen jokaiselle kohtion ja hidastinkalvon väliselle etäisyydelle differentiaalisella hajoamiskäyrämenetelmällä, joka huomioi syöttävien tilojen elinaikojen vaikutuksen.

Tulokseksi saatiin, että ^{182}Pt:n ensimmäisen 4^+-viritystilan keskimääräinen elinaika on
$\tau = 40,8(14)$ ps. Tämä vastaa siirtymätodennäköisyyttä $B(E2) = 221(8)$ W.u. Olettemalla, että ydin pyörii akselin suhteen symmetrisesti saadaan siirtymäkvadrupolimomentiksi $|Q_t| = 6,90(12)\, e$b.

Kvadrupolimomenttia voidaan verrata muiden $N = 104$ isotoonien prolaattien 4^+-viritystilojen kvadrupolimomentteihin. Vaikka kvadrupolimomentin varausriippuvuus otetaan huomioon, on platinan 4^+-tilan kvadrupolimomentti selkeästi pienempi kuin ^{186}Pb:n 4^+-tilan kvadrupolimomentti. Lisäksi kvadrupolimomentit pienenevät, kun ytimien varausluku pienenee. Ennen kuin ^{182}Pt:n viritystilojen kollektiivisuudesta voidaan kuitenkaan päätellä enempää, täytyy määrittää muiden matalaenergisten viritystilojen kvadrupolimomentit.
finnish

Contents

Chapter 1

Introduction

Many α- and β-decays leave the daughter nucleus in an excited state. Also most nuclear reactions populate excited states in the produced nuclei. An excited state can decay to the ground state or a lower lying excited state via an electromagnetic transition, which proceeds via a γ-ray emission or internal conversion. In some cases an α- or β-decay can proceed directly from an excited state.

For nuclear states with lifetimes of the order of nanoseconds or longer (isomeric states), a direct measurement can be employed and the time between the detected γ-rays can be measured. The time resolution of the detector system sets a lower limit for lifetimes which can be determined this way. For shorter lifetimes indirect measurements have to be employed. In this work the Recoil Distance Doppler-Shift method is used to measure the lifetime of the yrast 4^+ state in ^{182}Pt.

Chapter 2

Theoretical background

2.1 General properties of electromagnetic transitions and shape deformation

An electromagnetic transition is characterized with its type, electric or magnetic and the multipole of the associated radiation field. The multipole L must fulfill the selection rule

$$|I_i - I_f| \leq L \leq I_i + I_f,$$

where I_i and I_f are the angular momenta quantum numbers of the initial and final states. No $L = 0$ electromagnetic transition via a single photon emission is possible because of the properties of the corresponding operators [1]. The type of the transition depends on the parities of the initial and final state, π_i and π_f respectively, and the multipolarity of the transition:

$$\pi_i \, \pi_f = (-1)^L \text{ for electric transition}$$
$$\pi_i \, \pi_f = (-1)^{L+1} \text{ for magnetic transition.}$$

In general the lowest possible multipole is favoured, with the exception of $E2$ transitions competing with $M1$ transitions in a collective nucleus.

The transition probability between states $|\xi_i, I_i\rangle$ and $|\xi_f, I_f\rangle$ is given by

$$\lambda_{fi}^{(\sigma L)} = \frac{2}{\epsilon_0 \, \hbar \, L} \frac{L+1}{[(2L+1)!!]^2} \left(\frac{E_\gamma}{\hbar c} \right)^{2L+1} B(\sigma L; \, \xi_i \, I_i \rightarrow \xi_f \, I_f). \tag{2.1}$$

Here σ is the type of the transition and E_γ the transition energy. ξ_i and ξ_f supply the other quantum numbers except the angular momentum of

the corresponding states and $B(\sigma L;\, \xi_i\, I_i \rightarrow \xi_f\, I_f)$ is the reduced transition probability,

$$B(\sigma L;\, \xi_i\, I_i \rightarrow \xi_f\, I_f) = \frac{1}{2I_i+1}|(\xi_i\, I_i||M(\sigma L)||\xi_f\, I_f)|^2, \tag{2.2}$$

where $M(\sigma L)$ is the electromagnetic operator. The transition probability is also called decay constant when it is used in the exponential decay law.

The mean lifetime of the state is related to the transition probability by

$$\tau = \sum_f \frac{1}{\lambda_{fi}}, \tag{2.3}$$

where all possible final states are taken into account. Thus, the $B(\sigma L)$ value can be calculated, if the lifetime and the excitation energy are known. For $E2$ transitions Eq. 2.1 and Eq. 2.3 reduce to

$$B(E2) = \frac{0.0816}{\tau E_\gamma^5(1+\alpha_{\mathrm{tot}})}\, e^2\mathrm{b}^2, \tag{2.4}$$

when E_γ is given in MeV and τ in picoseconds. α_{tot} is the coefficient of total internal conversion.

As the electromagnetic operators are well known, the transition probability gives information about the wave functions of the initial and final states. Usually the transition probabilities are expressed in Weisskopf units. The Weisskopf unit is an estimate for a single-particle transition. $B(E2)$ values that are considerably larger than the Weisskopf estimate correspond to collective transitions, while lower values indicate a poor overlap of the initial and final state wave functions.

For an axially symmetric rotating nucleus the transition probability can also be expressed as a function of the transition quadrupole moment Q_t. For an $E2$ transition the transition probability can be written as [2]

$$B(E2; I_i \rightarrow I_f) = \frac{5}{16\pi}\, e^2 Q_t^2\, \langle I_i\, 0\, 2\, 0 | I_f\, 0\rangle^2\,. \tag{2.5}$$

The transition quadrupole moment equals to the intrinsic quadrupole moment Q_0 for purely rotational states within the same band [3]. The intrinsic quadrupole moment can be written in terms of the electric matrix element or the electric operator as

$$\begin{aligned} Q_0 &= \sqrt{\frac{16\pi}{5}}\, \mathcal{M}(E2) \\ &= \sqrt{\frac{16\pi}{5}}\, (\xi\, I||M(E2)||\xi\, I). \end{aligned} \tag{2.6}$$

Rotational structures can be observed only in nuclei which have non-spherical equilibrium shapes. The shape is described by

$$R(\theta,\, \phi) = R_{\mathrm{av}} \sum [1 + \beta_\mu Y_{\mu 0}(\theta, \phi)], \tag{2.7}$$

where $R_{\mathrm{av}} = A^{1/3} R_0$, $R_0 = 1.2$ fm, β_μ are the deformation parameters and $Y_{\mu 0}(\theta, \phi)$ the spherical harmonics. It can be noticed that there is no ϕ-dependence in the radius, so the nucleus remains cylindrically symmetric.

Sometimes it is enough to only take the quadrupole deformation into account. Hence, β_2 is normally called the deformation parameter, which describes the eccentricity of a rotating ellipsoid:

$$\beta_2 = \frac{4}{3}\sqrt{\frac{\pi}{5}}\,\frac{\Delta R}{R_{\mathrm{av}}}. \tag{2.8}$$

Here ΔR is the difference between major and minor axes of the ellipsoid. For a prolate (rugbyball shaped) nucleus $\beta_2 > 0$, while for an oblate (pancake shaped) nucleus $\beta_2 < 0$.

Besides the deformation parameter the moment of inertia is used when describing the deformation and collectivity of a nucleus [4]. The excitation energy of states within a rotational band can be written with respect to the lowest state of the band in terms of the moment of inertia $\mathcal{J}$ as,

$$E = \frac{\hbar^2}{2\mathcal{J}}\, I(I+1). \tag{2.9}$$

With different models for the motion of nuclear matter inside the nucleus the moment of inertia can be written as a function of the deformation parameter. Assuming that the nucleus behaves like a rigid body the moment of inertia can be written as

$$\mathcal{J} = \frac{2}{5}\, M R_{\mathrm{av}}^2 (1 + 0.31\beta_2), \tag{2.10}$$

where M is the mass of the nucleus. These equations link the γ-ray energies directly to the deformation of the band.

For a rotating deformed nucleus the quadrupole moment can be observed. In the rest frame of the nucleus the intrinsic quadrupole moment can be written as

$$Q_0 = \frac{3}{\sqrt{5\pi}}\, R_{\mathrm{av}}^2 Z \beta_2 (1 + 0.16\beta_2). \tag{2.11}$$

It can be seen from Eq. 2.6 and Eq. 2.10 that the intrinsic quadrupole moment is proportional to the deformation parameter in the leading order, while the

kinetic moment of inertia is not. Hence the quadrupole moment is a better measure of nuclear collectivity. Therefore, measuring the lifetimes of the excited states directly gives information about the deformation, if it can be assumed that the nucleus is cylindrically symmetric and only rotating.

2.2 Collectivity in Pb, Hg and Pt nuclei near the $N = 104$ neutron mid-shell

The low-energy part of the yrast line in neutron-deficient even-even Pb, Hg and Pt isotopes is formed by a prolate band. While Pb and Hg nuclei have a spherical ground state, the prolate 0^+ state becomes the ground state in the Pt nuclei around the $N = 104$ neutron mid-shell. The energy level systematics of Pt isotopes and ground state deformations obtained from laser spectroscopy are illustrated in Fig. 2.1.

The prolate intruder band in Pb, Hg and Pt nuclei around $N = 104$ neutron mid-shell is usually associated with $\pi(np-mh)$ excitations across the $Z = 82$ shell gap. These excitations are lowered in energy because the additional $\pi-\nu$ coupling is strong and attractive [2]. The coupling strength should depend on the number of valence neutrons (particles or holes). At the neutron mid-shell, where the number of valence neutrons is highest, the coupling should have it's maximum. Also the number of valence protons should have an effect on the coupling strength and hence the collectivity, which should within this simple picture increase when moving from Pb nuclei to Hg and further to Pt as the number of valence protons increases.

Fig. 2.2 shows the kinetic moments of inertia for several nuclei around the neutron mid-shell as well as the energies of γ-ray transitions within the prolate band for $N = 104$ nuclei ^{182}Pt, ^{184}Hg and ^{186}Pb. No dependence on Z or N can be observed in the moments of inertia within the prolate band. Also the γ-ray energies are similar for the $N = 104$ isotones. These similarities do not agree with the $\pi(mp - nh)$ intruder picture (intruder-spin concept [6]) as the Pb, Hg and Pt bands are all similar. They are also difficult to explain with the number of valence protons and neutrons. As the moments of inertia are not very sensitive to collectivity, it is necessary to determine the transition quadrupole moments to obtain more information about the collectivity and structure of these bands.

The transition quadrupole moments extracted from the lifetime measurements for prolate states are shown for several Pb, Hg and Pt isotopes in

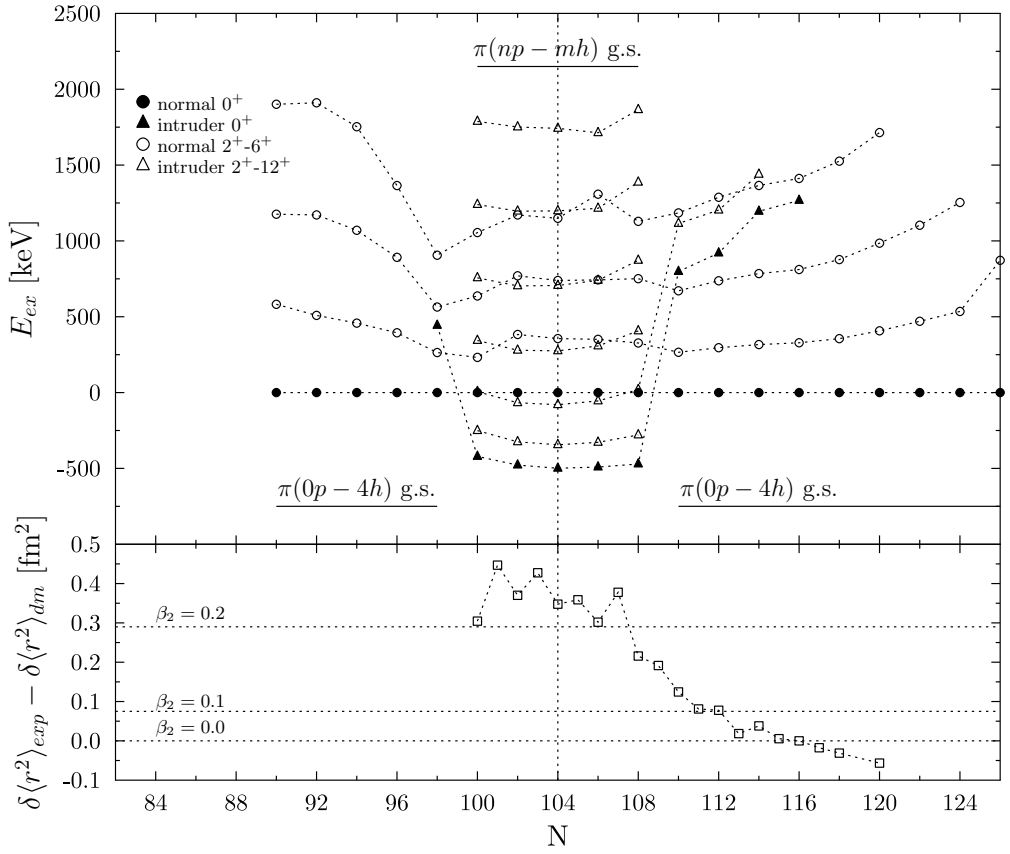

Figure 2.1. Radii and energy level systematics for Pt nuclei. The radii data from laser spectroscopy shows the deviation of the measured root mean square radius from the value of the droplet model. The 0^+ ground state at high ($N > 110$) neutron numbers has an almost spherical shape. This state is associated with $\pi(0p-4h)$ configuration. The intruder band which comes down in energy at the neutron mid-shell $N = 104$ has a prolate shape and is associated with the $\pi(np-mh)$ excitation. The energy levels have been normalized with respect to the $\pi(0p-4h)$ configuration 0^+ state. Figure taken from [5].

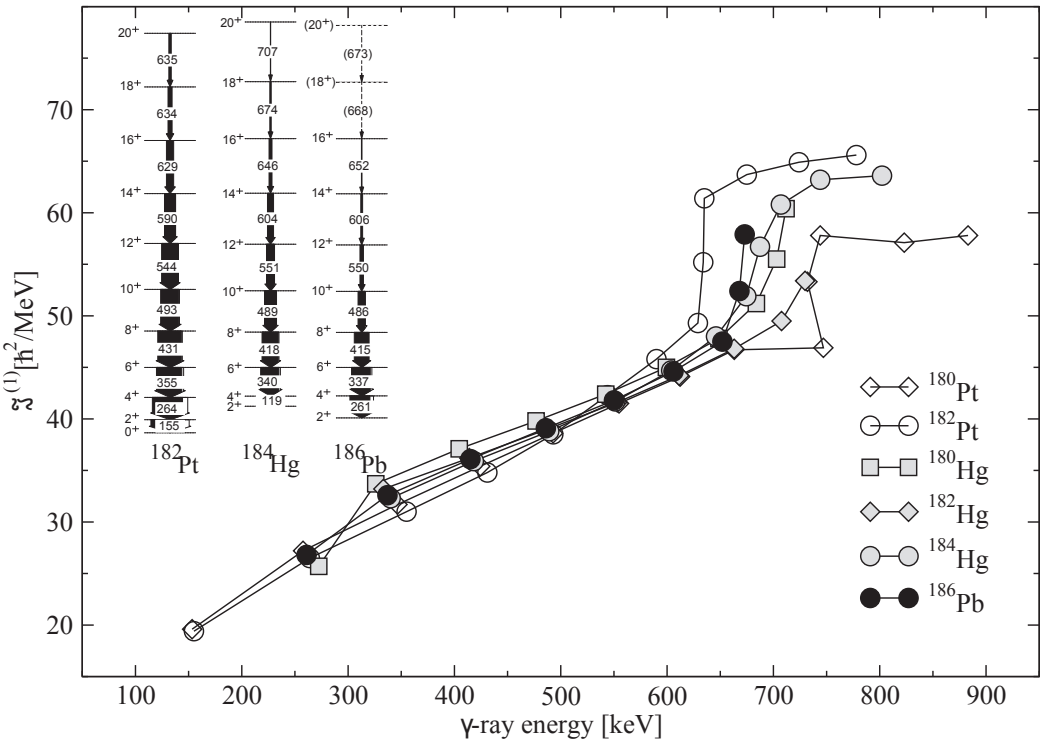

Figure 2.2. Kinematic moment of inertia as function of γ-ray energy for yrast states in ^{180,182}Pt, ^{180,182,184}Hg and ^{186}Pb. The inset shows the corresponding energy levels for the $N = 104$ isotones. Figure taken from [7].

Fig. 2.3. There is evidence that collectivity decreases when moving from Pb nuclei to Hg even though the moments of inertia presented in Fig. 2.2 are almost identical.

One possible theory to explain the decreasing collectivity with decreasing Z is to assume that the nuclei have a triaxial shape instead of an ellipsoid. This would imply that the the transition quadrupole moment would not equal to the intrinsic quadrupole moment.

In this work the lifetime of the yrast 4^+ state in ^{182}Pt was determined. Together with lifetimes for other excited states, which can be obtained from the same data as analyzed in this work, information about collectivity in neutron mid-shell nuclei with lower Z is obtained. The transition quadrupole moments can be compared to other $N = 104$ nuclei ^{186}Pb and ^{184}Hg to confirm the decreasing collectivity when moving to lower Z.

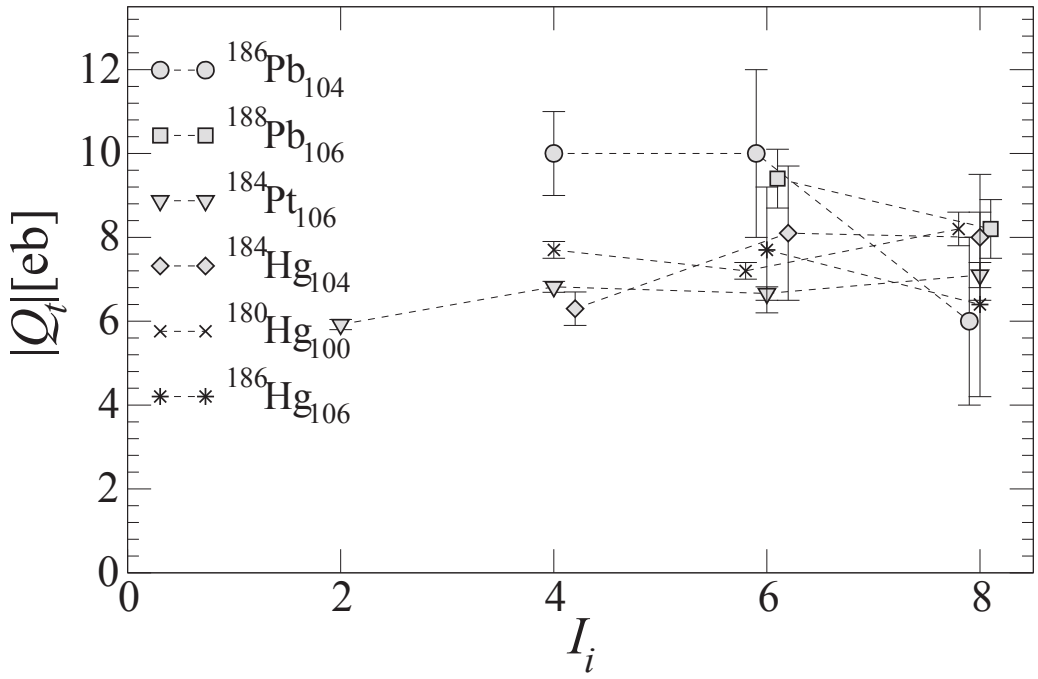

Figure 2.3. Transition quadrupole moments extracted from the lifetime measurements in ^{186,188}Pb [8], ^{180}Hg [9], ^{184,186}Hg [10, 11] and ^{184}Pt [12]. Some $|Q_t|$ values have a slight offset to the I_i to maintain the clarity of the presentation.

Chapter 3

Experimental methods

Prompt γ-ray spectra of ^{182}Pt were recorded at 11 target-to-degrader distances ranging from 5 μm to 4000 μm. The studied excited states of ^{182}Pt were populated via the fusion-evaporation reaction ^{100}Mo(^{86}Kr, 4n)^{182}Pt. The beam was provided by the K-130 cyclotron. The beam energy was 345 MeV and the intensity was $1.6 - 2.2$ pnA.

A 1.2 mg/cm^2 thick Mo target was used and the recoil velocity was 0.0346(11) c. A magnesium foil with a thickness of 1.1 mg/cm^2 was used as a degrader. It reduced the velocity of the recoils to 0.0255(11) c. The velocities have been calculated from the observed Doppler shifts of γ-ray energies.

3.1 The Recoil Distance Doppler-Shift method

The basic principle of the Recoil Distance Doppler-shift (RDDS) method is that the observed γ-ray energy depends not only on the energy of the related γ-ray transition, but also on the velocity of the nucleus emitting the γ-ray and the angle between the velocity of the nucleus and the detector. The non-relativistic Doppler shift for the observed γ-ray energy is defined by

$$E = E_0 \left(1 + \frac{v}{c} \cos\theta\right), \tag{3.1}$$

where E_0 is the energy of the transition, v the velocity of the nucleus emitting the γ-ray and θ the angle between the velocity of the nucleus and the detector. So, if the angle can be measured or is otherwise known, the observed γ-ray energy gives the velocity of the nucleus when the energy of the γ-ray transition is also known.

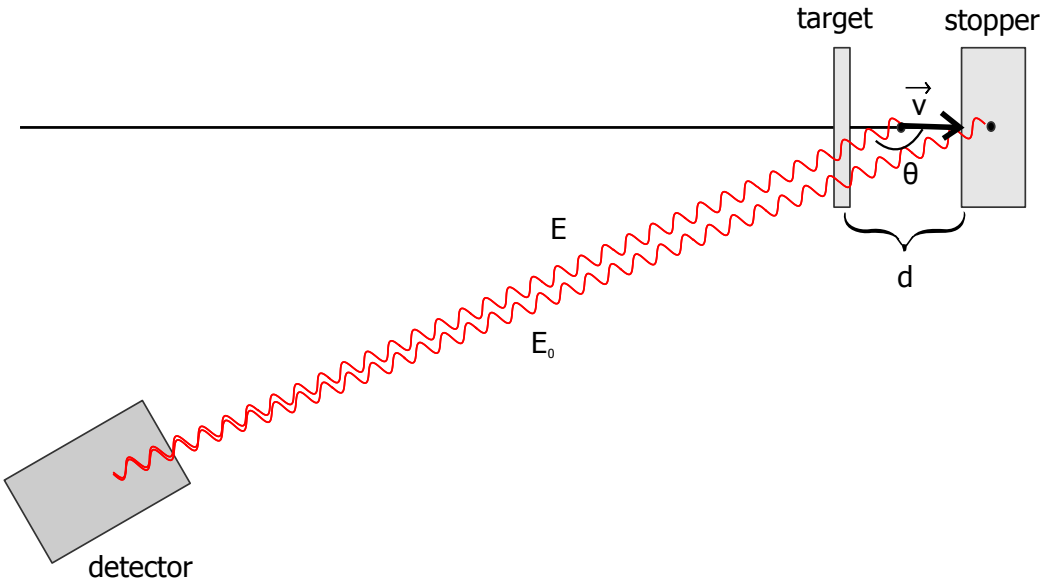

Figure 3.1. The energy of the observed γ ray depends on the velocity of the emitting nucleus and the angle between the velocity of the nucleus and the detector. By measuring the intensities of the γ-rays emitted from the stopped nuclei and of those which are still in flight at several target-to-stopper distances the lifetime of the related energy level can be determined.

In the Recoil Distance Doppler-Shift method, nuclei are created in nuclear reactions when the beam hits the target. After this they are implanted into a stopper. The situation is illustrated in Fig. 3.1.

The shift in the energies of the γ-rays emitted from the nuclei in flight and from the stopped nuclei can be measured. The time-of-flight between the target and the stopper can be calculated because the velocity of the nuclei is known. The intensity of the shifted and unshifted γ-rays are measured as a function of the distance between the target and the stopper. By plotting the intensity of the shifted peak, i.e. the amount of nuclei decaying before the stopper, normalized by the total amount of decays observed as a function of the distance, the lifetime can be obtained by fitting a sum of exponential curves or by analyzing the data with Differential Decay Curve Method, see section 4.3.

When using nuclear reactions with small cross sections one has to invent ways to clear the γ-ray spectrum from the orders of magnitude larger background, which is created by fission and other reaction channels. One effective way is to analyze $\gamma\gamma$-coincidences, i.e. events with at least two consecutive γ-rays. This is also necessary in order to eliminate the effect of the lifetimes of the

feeding states on the lifetime of the state of interest.

With fusion-evaporation reactions, like the one used in this work, the γ-ray spectrum is usually obtained by gating with recoils that are observed at the focal plane of the separator (see section 4.1). This requires that the stopper used in the RDDS measurements is replaced by a degrader, which slows the recoils down, but also allows them to pass through.

Using the degrader makes it possible to use fusion-evaporation reactions with small cross sections and tag γ-rays with recoils or even with their decays. However, the shift in the energy is smaller and hence the separation of the shifted and degraded components is not so good. Also, the small angle scattering of the recoils in the degrader reduces the transmission of the separator. The material and thickness of the degrader have to be optimized so that the shift in the energy is large enough so that the peaks in the γ-ray spectrum can be separated, but with a large enough number of recoils still passing through the separator.

The advantage of the fusion-evaporation reactions in the RDDS measurements is that the evaporation residues recoil approximately to the same direction as the beam. The small angle scattering in the target and the degrader foil does not need to be taken into account when calculating the angle between the flight direction of the ion and detector as it can be assumed to equal to the angle between the beam direction and the detector.

3.2 Experimental set-up

The experimental set-up consisted of the JUROGAM II germanium detector array at the target position, the gas-filled separator RITU, the focal-plane detector set-up GREAT and the Köln plunger device at the target position. JUROGAM, RITU and GREAT are shown in Fig. 3.2.

3.2.1 Köln plunger

The Köln plunger device [13–15] replaced the normal JUROGAM II target chamber. The plunger houses the target and the degrader (or stopper) foils, so that the distance between the target and the degrader can be accurately measured and changed. In the Köln plunger the position of the degrader is fixed and the target can be moved from direct contact to 8000 μm apart

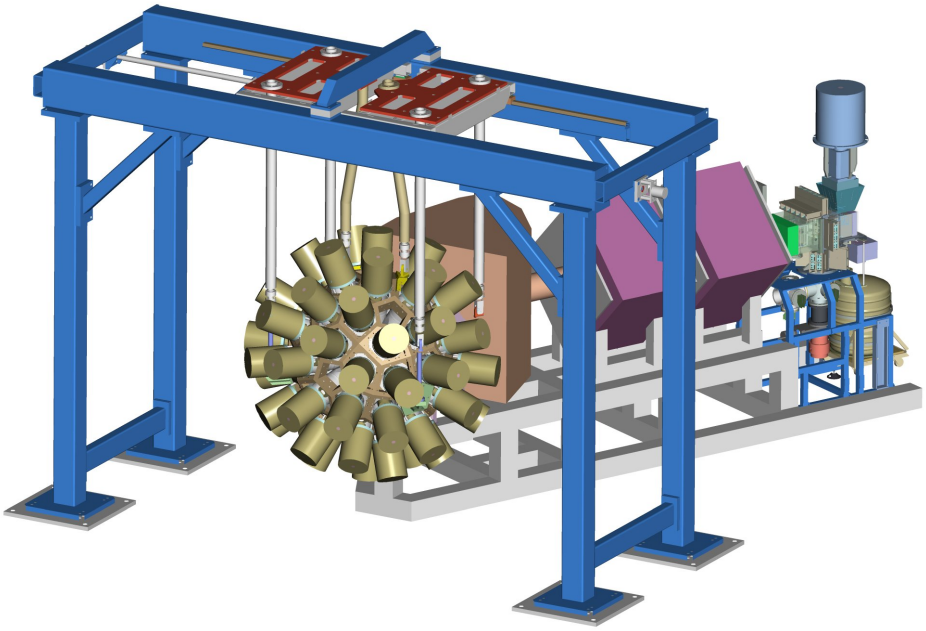

Figure 3.2. A schematic drawing of JUROGAM, RITU and GREAT. Courtesy of Dave Seddon.

with a linear Inchworm motor, which is based on piezo crystals. The foils are attached to aluminum rings and stretched over conical support rings. The support rings are mounted on another set of frames which are connected to the rods inside the device as parallel as possible.

The distance between the thin foils close to each other cannot be measured mechanically. The long distances are measured with an optical structure attached to the Inchworm. For short distances (shorter than 200 μm) the distance is measured with a TESA magnetic transducer when the system is cold. The heat deposit of the beam leads to stretching of the foils and bearings making distance measurement like this impossible. The distance is measured as the capacitance between the foils in beam and the system is calibrated off-beam with the TESA. From the calibration curve, mechanical and electric contact can usually be determined. The precise measurement of the contact is however not necessary when using the DDCM analysis.

A separate control system is used for adjusting the distance between the foils automatically at short distances. Adjusting the distance corrects the differences due to heat transfer from the beam or due to stretching of the

foils.

3.2.2 JUROGAM II

JUROGAM II is a germanium-detector array at the target position of RITU. It consists of 39 n-type high purity germanium detectors arranged so that they cover as a large solid angle as possible. 15 of the detectors are Eurogam phase I [16] or GASP type detectors [17] and 24 are Eurogam clover detectors [18]. All of the detectors have bismuth germanate (BGO) shields for Compton suppression.

The detectors are positioned in four rings, with all of the detectors in each ring having the same angle with respect to the beam direction. This means that all of the detectors in one ring observe the same Doppler shift of γ-ray energies. The Phase1 and GASP detectors are situated in rings 1 (5 detectors) and 2 (10) and the clover detectors in rings 3 (12) and 4 (12). The angle with respect to the beam direction is 157.6° for ring 1, 133.57° for ring 2, 104.5° for ring 3 and 75.5° for ring 4. Only with the detectors in ring 1 and 2 large enough Doppler shifts in γ-ray energies can be observed, so that they can be used for RDDS measurements. The other two rings were used for gating in $\gamma\gamma$-coincidence analysis.

The average resolution of the detectors is $2.5 - 4$ keV for 1.3 MeV γ-rays. In the measurements the resolution was worse because of Doppler boardening.

The absolute peak efficiency of the array for 1.3 MeV γ-rays is approximately 6% in normal in-beam measurements. In plunger measurements, only the first two rings have suitable angles to observe Doppler shifts neccessary for the RDDS measurement. This reduces the efficiency considerably even though the other rings can be used for gating.

3.2.3 Recoil separator RITU

RITU (Recoil Ion Transmission Unit) is a gas-filled separator [19] used to separate the fusion-evaporation reaction products from fission fragments, beam and target like products and the primary beam. The magnetic structure is $QDQQ$, where the first quadrupole (Q) focuses the ions to better match the aperture of the following dipole (D). The last quadrupoles focus the reaction products to the focal plane.

In a vacuum-mode separator usually only one or two different charge states can be delivered to the focal plane, as ions with different charges have different trajectories in the magnetic field of the dipole according to

$$B\rho = \frac{p}{q} \approx \frac{mv}{q}, \tag{3.2}$$

where B is the magnetic field strength, ρ the radius of curvature, p the momentum and q the charge of the ion. On the other hand, the vacuum enables mass resolution.

In gas-filled separators the mass resolution is lost, but low pressure helium gas makes the ions to have an average charge state, which is independent of their initial charge state. The trajectory of the ion in a magnetic field can be calculated with this average charge state. This enables transferring more reaction products to the focal plane. Now Eq. 3.2 can be written as

$$B\rho \approx \frac{mv}{q_{\mathrm{ave}}} = \frac{mv}{{}^{v}/_{v_0}\, Z^{1/3}} = 0.0227\mathrm{A/Z}^{1/3}\ \mathrm{Tm}, \tag{3.3}$$

where v_0 is the Bohr velocity, $v_0 = 2.19 \cdot 10^6$ m/s.

3.2.4 The focal plane spectrometer GREAT

The focal plane spectrometer GREAT (Gamma Recoil Electron Alpha Tagging) [20] comprises silicon, germanium and gas detectors. It is dedicated to studying decays of reaction products, but can be used as well for tagging the prompt γ-rays at the target position.

A transmission multiwire proportional counter (MWPC) is situated at the entrance of GREAT. The entrance and exit windows are 131 mm wide and 50 mm high and made of Mylar foil. They separate the helium gas inside RITU from the isobutane used inside the MWPC and the vacuum needed for other GREAT detectors. The MWPC is mainly used for separating the α particles from the recoils and further the recoils from the scattered beam particles.

After the gas detector the recoils are implanted in the double-sided silicon strip detectors (DSSDs). There are two DSSDs, both 40 mm high and 60 mm wide, separated by a 5 mm gap. Separating the recoils from the scattered beam can be done by combining the energy loss in the gas detector with the time-of-flight between the JUROGAM and the MWPC or between the

MWPC and the DSSD. The DSSDs are position sensitive detectors and therefore the subsequent α-decay can be correlated with the arrival of the ion.

The other detectors of the GREAT are PIN-diodes, used for detecting β- and α-particles and conversion electrons and germanium detectors used for detecting γ-rays from isomeric states subsequent to charged particle decay and X-rays. As these detectors were not used in this study, they are not described here further. For details, see [20].

3.3 Data Acquisition

In data acquisition a triggerless Total Data Readout (TDR) system [21] was used. The TDR system has been designed for Recoil Decay Tagging (RDT) [22] experiments. In the TDR all of the channels are read independently and time-stamped with 100 MHz clock signal. The events are later constructed in the software with spatial and temporal correlations.

Chapter 4

Data analysis

A partial level scheme of ^{182}Pt is shown in Fig. 4.1. The choice of reaction and set-up enabled either analyzing the data as stand alone $\gamma\gamma$-data, or using the recoils for tagging. As the α-decay branch of ^{182}Pt is quite weak contributing to only 4.84% of the ground-state decay and the half-life is 2.6 minutes, no recoil-decay tagging was possible. However, as the largest cross-section in the reaction was for ^{182}Pt and ^{183}Pt, most of the recoils were from one of these nuclei. Therefore, tagging the prompt γ-rays with recoils detected at the RITU focal plane provided sufficiently clean γ-ray spectra.

The spectra and matrices were constructed with the software package Grain [23].

4.1 Using recoils for tagging

Using recoils for tagging can be done with two different tagging methods. In the first one the time of flight between the MWPC and the DSSD is used together with the energy loss in the MWPC. When these are plotted in a matrix the recoils can be identified from the scattered beam particles.

The efficiency of the MWPC is a bit larger than that of the DSSD because of the geometry of the detectors. As only the time signal from the DSSD is used it is also possible to use the time of flight between JUROGAM and the MWPC instead of the time of flight between the MWPC and the DSSD. The time information was used together with the energy loss in the MWPC and the recoils were identified from the matrix as shown for time of flight between JUROGAM and the MWPC in Fig. 4.2.

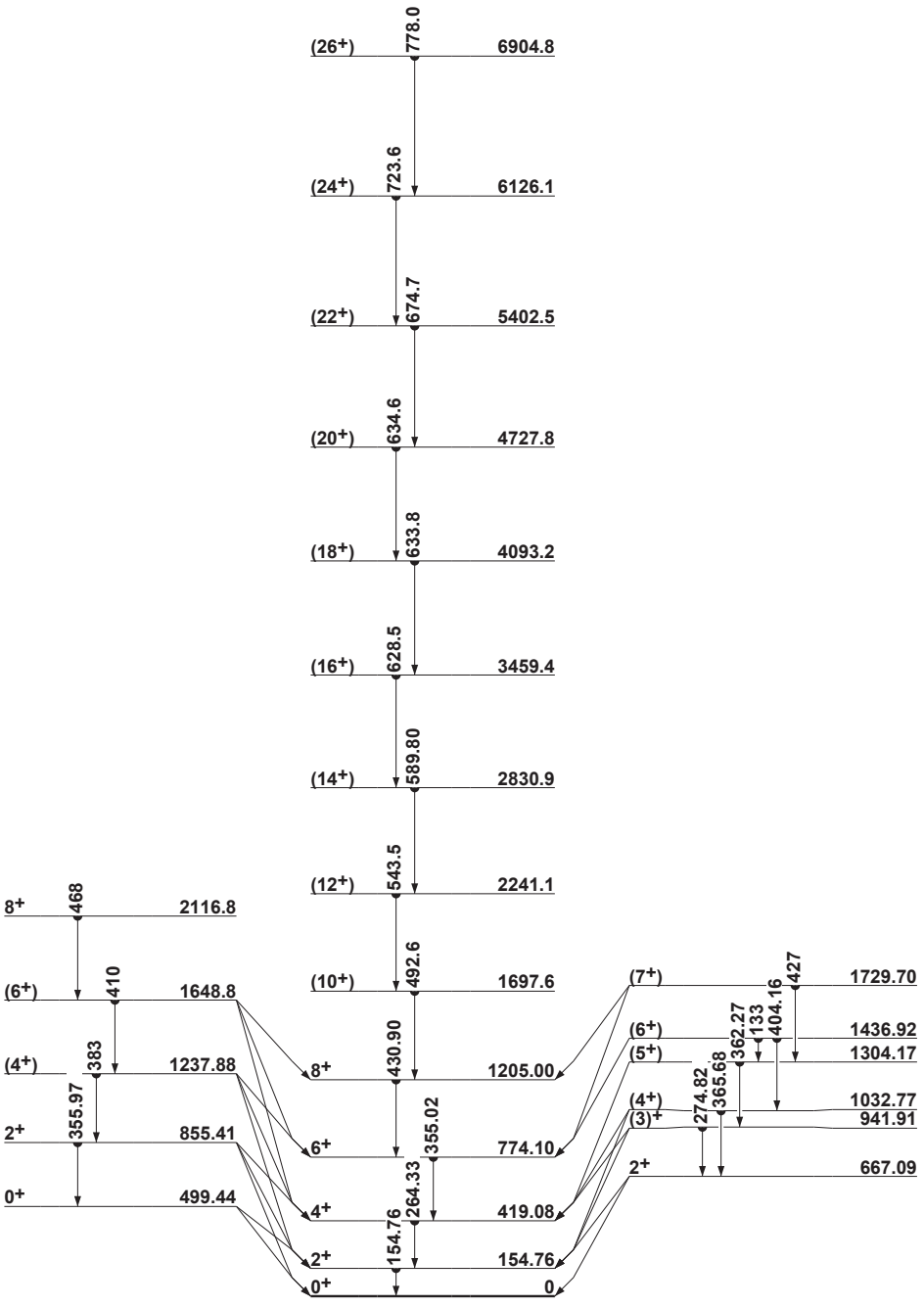

Figure 4.1. Partial level scheme of ^{182}Pt presenting the transitions relevant to this work [24].

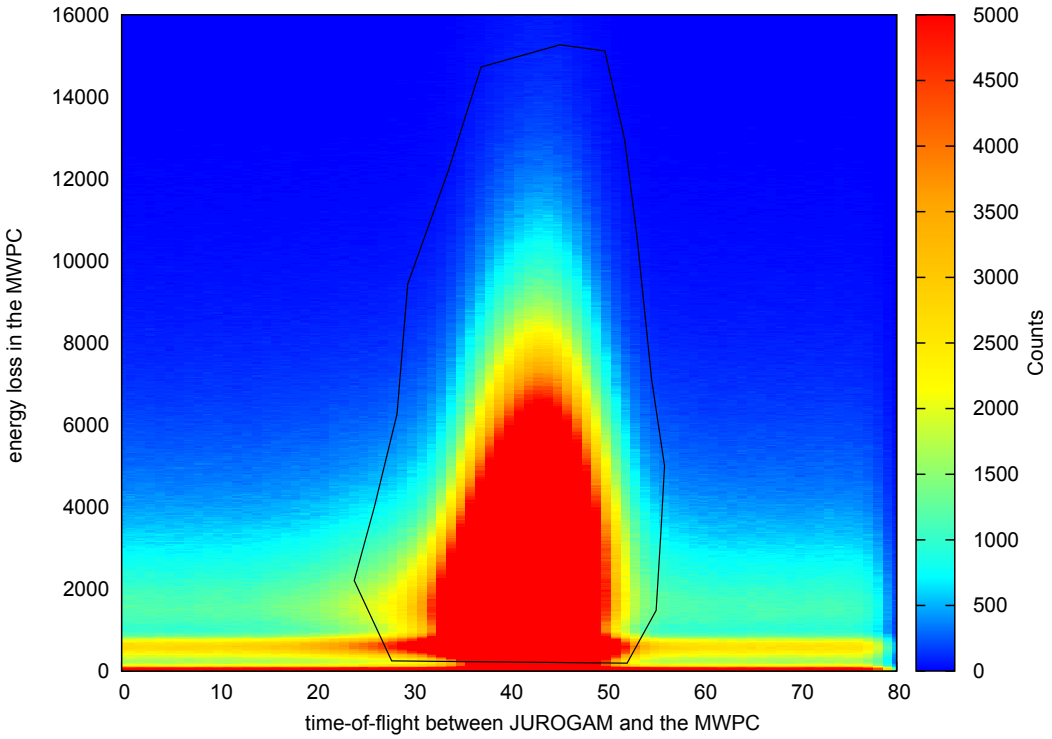

Figure 4.2. Time-of-flight between JUROGAM and the MWPC plotted against the energy loss in the MWPC. The two dimensional gate for identification of the recoils is marked to the picture.

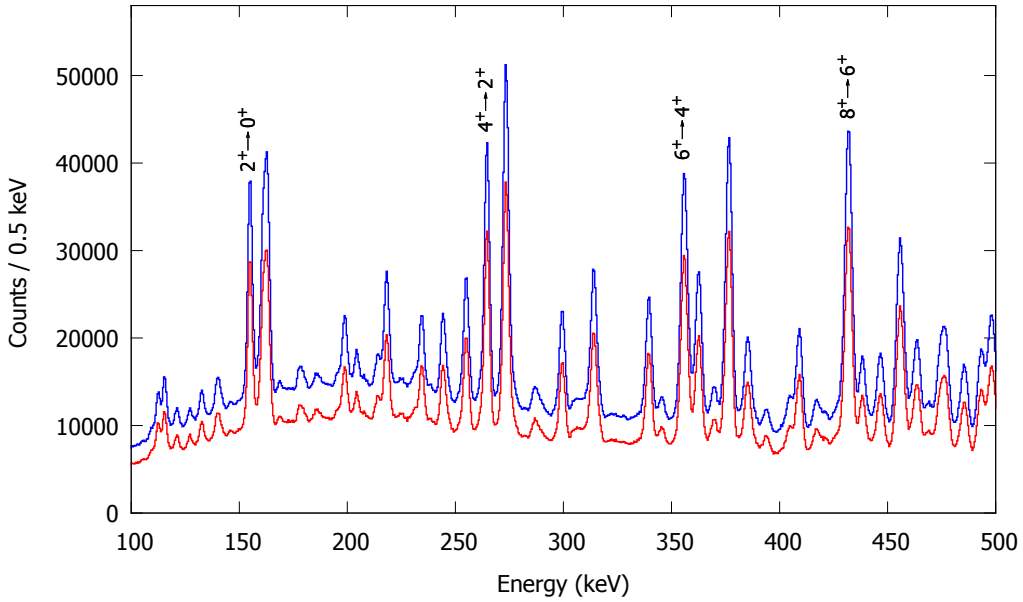

Figure 4.3. The recoil-gated singles JUROGAM spectra obtained by triggering with the MWPC signal and using two dimensional gate on the energy loss in the MWPC and the time of flight between JUROGAM and the MWPC (blue line) or between the MWPC and the DSSD (red line). The peaks corresponding to the γ-ray transitions in ^{182}Pt are marked.

Also different triggering methods were tested. Besides triggering with any event on the focal plane also triggering with just the MWPC was tested. The trigger which accepted all of the events at the focal plane gave a signal also when an α decay happened, which on the other hand, did not give a real γ-event at the target. As no data of the decays was needed for the sorting this resulted in more background.

These two tagging methods and triggering possibilities were compared by plotting the same data and looking at the resulting recoil gated JUROGAM spectra. It was found that when the time of flight between the MWPC and the DSSD was used for identifying the recoils no big difference was obtained with different triggering methods, except that the DSSD in a little more background. When using the time of flight between JUROGAM and the MWPC, triggering with the MWPC signal resulted in more data and less background, than triggering with the DSSD. This can be mostly explained by the size of the detectors. The JUROGAM spectra obtained by triggering with the MWPC and using different ways to identify recoils are shown in Fig. 4.3. When comparing the areas of the peaks corresponding to the γ-

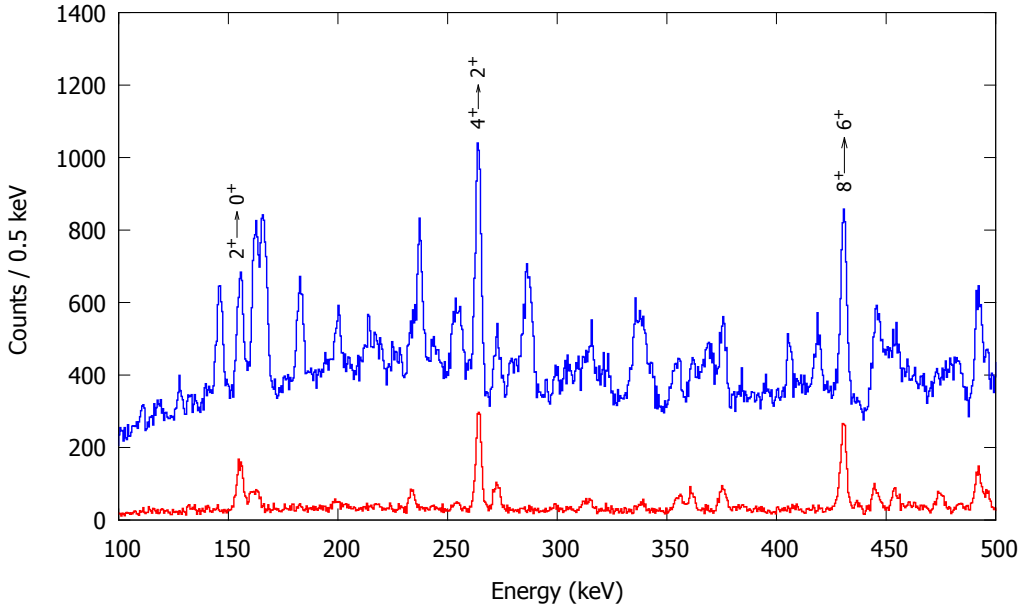

Figure 4.4. The spectrum obtained by gating on the $6^+ \rightarrow 4^+$ transition in the stand-alone $\gamma\gamma$ matrix (blue line) and also by requiring the recoil (red line). The peaks corresponding to the γ-transitions in ^{182}Pt are marked.

ray transitions of ^{182}Pt it was found out that by using JUROGAM-MWPC time difference in gating produced most data, approximately 25% more than using the time difference between the MWPC and the DSSD. The difference is what can be expected for this type of the reaction and is mostly explained by the size of the detectors.

4.2 Stand alone $\gamma\gamma$ analysis

The advantage of stand alone $\gamma\gamma$-data is the amount of statistics. The small-angle scattering in the degrader foil reduces the transmission of RITU. The magnesium degrader foil reduces the transmission approximately by a factor of two thirds [25]. The disadvantage of the stand-alone gamma-gamma data is the amount of background created mainly by the Coulomb excitation of the target and the beam and the γ-rays emitted from the fission fragments.

The spectrum obtained by gating on the $6^+ \rightarrow 4^+$ transition in the stand-alone $\gamma\gamma$ matrix and also by requiring the recoil detected at the focal plane are shown in Fig. 4.4. There are approximately three times more statistics

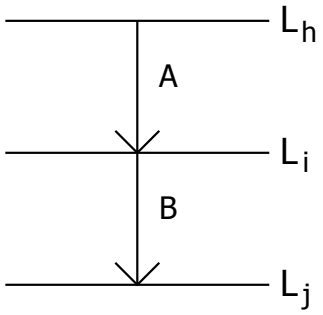

Figure 4.5. A schematic drawing of a decay scheme. Level L_{h} feeds the level of interest, L_{i}, via γ-ray transition γ_A and L_{i} decays to level L_{j} via γ-ray transition γ_B.

in the stand-alone $\gamma\gamma$-spectrum than in the one gated with the recoils. The further analysis was done with recoil-gated spectra because the recoil-gated spectrum is considerably cleaner.

4.3 The Differential Decay Curve Method

The Differential Decay Curve Method (DDCM) is a method for analysing RDDS data. Instead of fitting a sum of exponential curves to all distances, the lifetime is calculated separately for every distance. Also every level is analyzed separately with a first order differential equation. In principle the life-time can be calculated using only three measured target-to-degrader distances, while in practice measuring more distances is useful in detecting systematical errors. A complete derivation of the DDCM can be found in [26].

If level L_{i} is fed by a γ-ray transition from level L_{h} and is depopulated by a γ-ray transition to level L_{j}, the number of nuclei at the level L_{i} and L_{h} are related by

$$\frac{\mathrm{d}n_{\mathrm{i}}}{\mathrm{d}t} = -\lambda_{\mathrm{i}}\, n_{\mathrm{i}}(t) + \lambda_{\mathrm{h}}\, b_{\mathrm{hi}}\, n_{\mathrm{h}}(t), \tag{4.1}$$

where $n_{\mathrm{i}}(t)$ is the number of nuclei at state L_{i} at time t. λ_{i} and λ_{h} are the decay constants of levels L_{i} and L_{h} and b_{hi} is the branching ratio from level L_{h} to level L_{i}. The situation is illustrated in Fig. 4.5. In case of several feeding levels, L_{h}, they need to be summed over.

The lifetime of state L_i can be written as

$$\tau_\mathrm{i}(t) = \frac{-N_\mathrm{i}(t) + b_\mathrm{hi}\, N_\mathrm{h}}{\frac{\mathrm{d}}{\mathrm{d}t} N_\mathrm{i}(t)}, \tag{4.2}$$

where $N_\mathrm{i}(t) = \lambda_\mathrm{i} \int_t^\infty n_\mathrm{i}(t)\,\mathrm{d}t$, gives the number of nuclei at level L_i decaying after time t, and similarly for N_h. The N_i and N_h are proportional to the intensity of the degraded components at flight time $t = d/v$ [26].

The derivative $\frac{\mathrm{d}}{\mathrm{d}t} N_\mathrm{i}(t)$ can be determined by fitting a continuous analytical function $F(t)$ to the measured intensities and calculating its derivative. Another option is to estimate the derivative with the intensities measured at neighboring distances.

In principle, the lifetime can be determined from measured intensities of the degraded components at only a few distances. However, it is important to notice that to determine the lifetime accurately these distances must be inside the so called region of sensitivity. The region of sensitivity includes distances where both the numerator and the absolute value of the denominator of Eq. 4.2 are significantly larger than zero. Inside the region of sensitivity the lifetime can be determined accurately while outside of it the errors are larger.

When using Eq. 4.2 to calculate lifetimes the majority of the feeding intensity has to be observed. However, assumptions of the time behaviour of the unobserved feeding intensity can be made. This is not necessary if coincidence spectra are analyzed instead of singles. In a coincidence measurement it is possible to determine the lifetime τ_i by only taking into account one feeding level L_h. If the decay goes through $L_\mathrm{h} \rightarrow L_\mathrm{i} \rightarrow L_\mathrm{j}$ via γ-ray transitions A and B according to Fig. 4.5, the lifetime of L_i can be written as [26]

$$\tau_\mathrm{i}(t) = \frac{I_\mathrm{d}^{\mathrm{A(B)}}(t) - \alpha(t) I_\mathrm{d}^{\mathrm{B(A)}}(t)}{\frac{\mathrm{d}}{\mathrm{d}t} I_\mathrm{s}^{\mathrm{A(B)}}(t)}, \tag{4.3}$$

where

$$\alpha(t) = \frac{I_\mathrm{d}^{\mathrm{B(A)}}(t) + I_\mathrm{s}^{\mathrm{B(A)}}(t)}{I_\mathrm{d}^{\mathrm{A(B)}}(t) + I_\mathrm{d}^{\mathrm{A(B)}}(t)}. \tag{4.4}$$

$I_\mathrm{d}^{\mathrm{A(B)}}(t)$ denotes the intensity of the degraded component of the γ-ray transition A, gated with the γ-ray transition B. If gating only with the degraded/shifted component is possible Eq. 4.3 simplifies even further [26].

4.4 Lifetime of the first 4^+-state

The lifetime of the 4^+ state was determined from the recoil-gated $\gamma\gamma$-coincidence spectra. The recoils were identified with the time-of-flight between JUROGAM and the MWPC and the energy loss in the MWPC. The gate is presented in Fig. 4.2.

The $\gamma\gamma$-coincidence data was sorted separately for each distance. All four rings of JUROGAM were used for gating, and the intensities of the shifted and degraded components were studied with the first ring only. It is possible to repeat this for the second ring. Shifted and degraded components of the $4^+ \rightarrow 2^+$ transition were determined from spectra gated with the feeding $6^+ \rightarrow 4^+$ transition. The intensities of the components of the feeding transition were obtained from spectra gated with the $4^+ \rightarrow 2^+$ transition. Sample spectra are shown in Fig. 4.6. At the short distance (3 μm) only the degraded component can be observed, whereas at the long distance (4000 μm) only the shifted component is present. Unfortunately gating with $6^+ \rightarrow 4^+$ transition did not completely remove the peak of the ^{184}Pt $4^+ \rightarrow 2^+$ transition at 272.98 keV [24], but the energy difference of the transitions is large enough to separate the peaks in the fitting process.

The intensity difference of the degraded components of the feeding and depopulating transitions of the 4^+ state ($I_d^{\mathrm{A(B)}} - I_d^{\mathrm{B(A)}}$) and the intensity of shifted component of the depopulating transition ($I_s^{\mathrm{B(A)}}$) are presented in Fig. 4.7. The lifetime of the 4^+ state is calculated inside the region of sensitivity, which was deduced to be $60 - 1000$ μm. The lifetime of the 4^+ state was calculated from the measured intensities using the Napatau program [27]. The derivative of the shifted component was obtained by fitting few smoothly connected second order polynomials to the measured data points I_s. The fitted polynomials and their derivatives are also plotted in Fig. 4.7.

The obtained lifetimes inside the region of sensitivity are presented in Fig. 4.8. From the individual values the final result is calculated as a weighted mean, resulting in

$$\tau_{4^+} = 40.8(14) \text{ ps.}$$

Furthermore, the corresponding $B(E2)$ value can be calculated with Eq. 2.4 to be

$$B(E2; 4^+ \rightarrow 2^+) = 221(8) \text{ W.u.}$$

The value for the internal conversion coefficient (α_{tot}) has been obtained using the BrIcc calculator, [28] to be $\alpha_{\mathrm{tot}} = 0.1447(21)$. The transition quadrupole

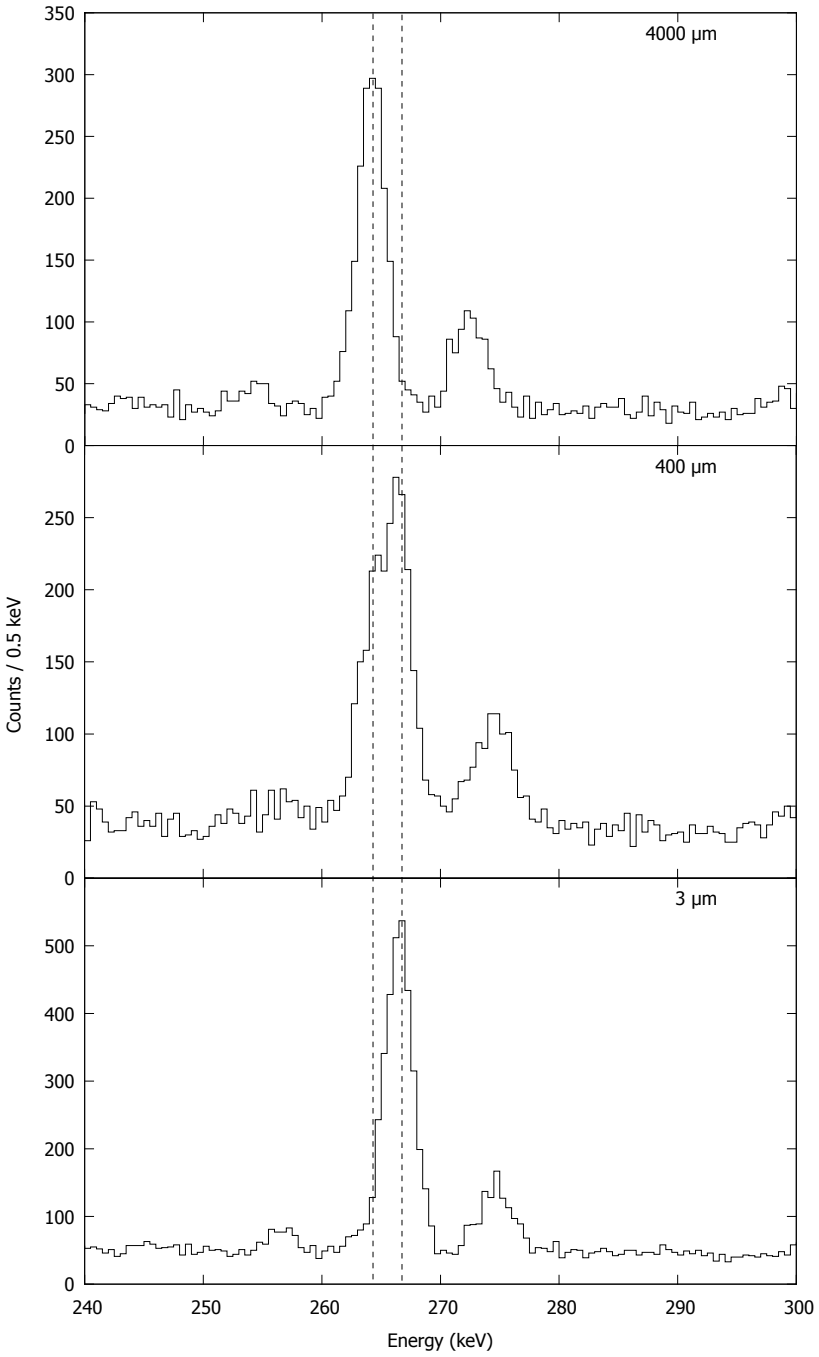

Figure 4.6. $\gamma\gamma$-coincidence spectra for the ^{182}Pt $4^+ \rightarrow 2^+$ transition gated with the directly feeding $6^+ \rightarrow 4^+$ transition at the target-to-degrader distances 3 µm, 400 µm and 4000 µm. The spectra are Doppler corrected with the velocity of the recoil after the target. The shifted component is on the left and the degraded on the right. The smaller peak at 273 keV originates from ^{184}Pt.

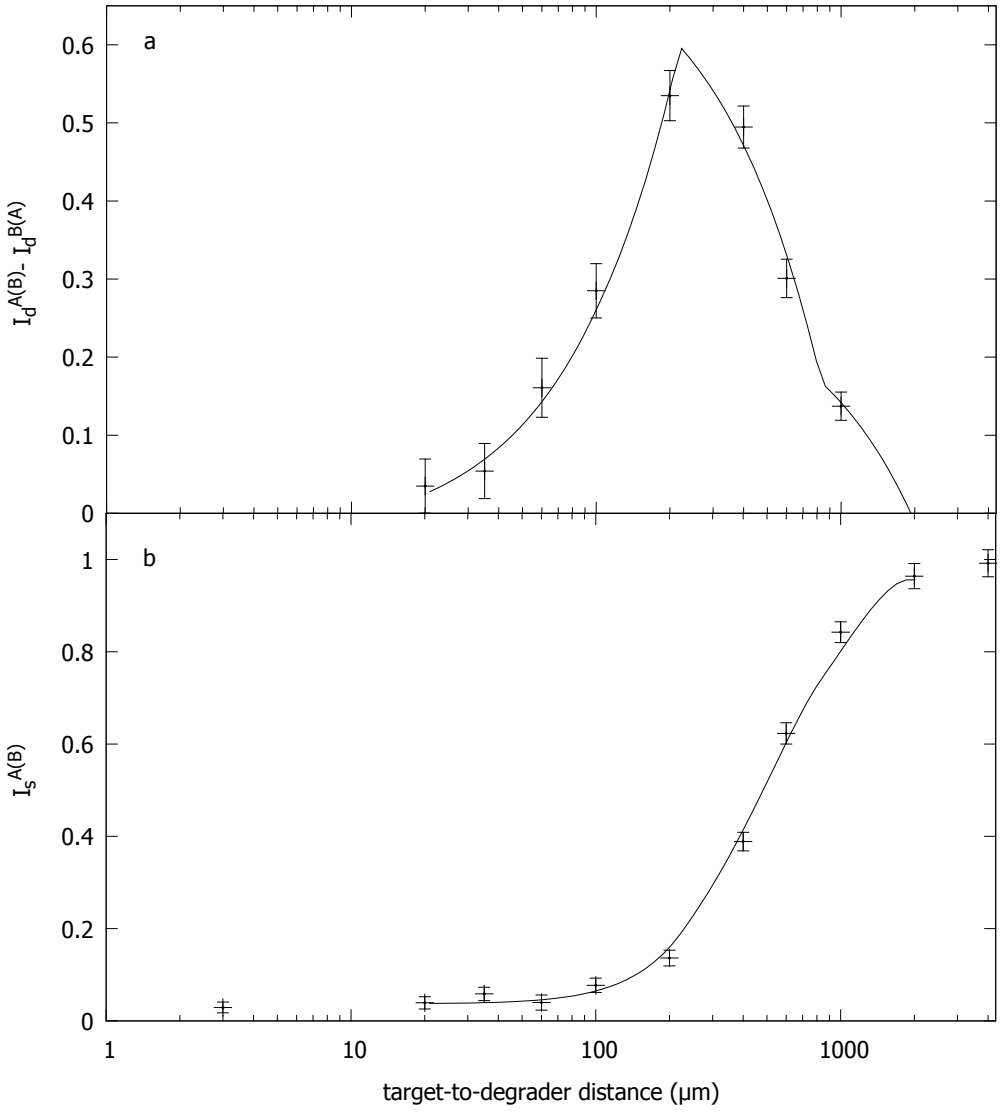

Figure 4.7. a) The intensity difference of the degraded components of the feeding and depopulating transitions of the 4^+ state ($I_d^{\mathrm{A(B)}} - I_d^{\mathrm{B(A)}}$) and b) the intensity of shifted component of the depopulating transition ($I_s^{\mathrm{B(A)}}$) as a function of target-to-degrader distance. All of the intensities have been normalized by the sum of the degraded and shifted intensity. The smoothly connected polynomials, which were fitted to the shifted intensities, are also plotted. Their derivative multiplied by τ is plotted with the degraded intensities.

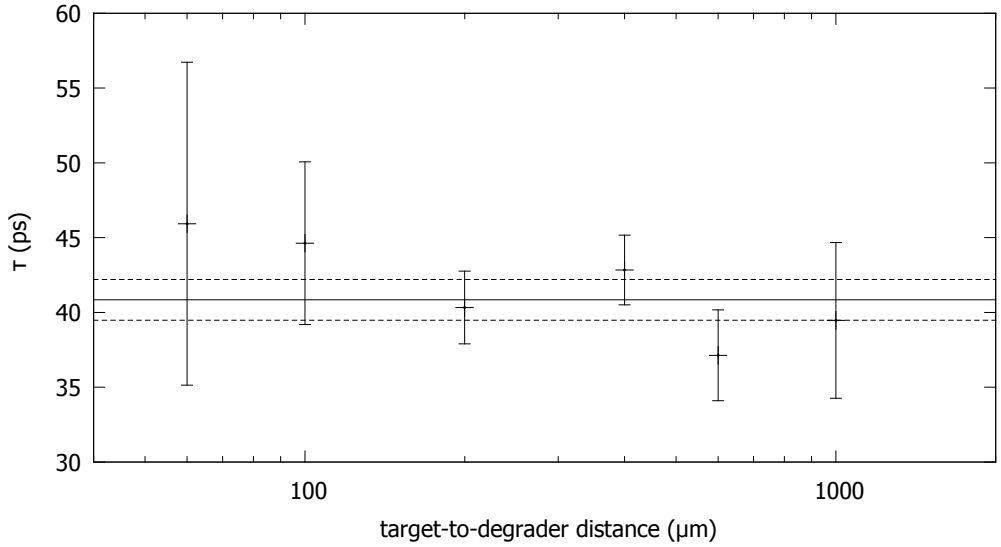

Figure 4.8. Lifetime of the 4^+ state obtained at different target-to-degrader distances. The final result is calculated as a weighted mean, $\tau_{4^+} = 40.8(14)$ ps.

moment can be calculated with Eq. 2.5 to be

$$|Q_t| = 6.90(12)\, e\mathrm{b}.$$

The sign of the quadrupole moment cannot be deduced from the measured lifetime as can be seen from Eq. 2.5. Assuming that the transition quadrupole moment equals to the intrinsic quadrupole moment, the deformation parameter can be calculated using Eq. 2.11. Inserting the quadrupole moment to the equation gives :

$$|\beta| = 0.243(4).$$

When calculating the errors only statistical uncertainties have been taken into account. For a complete analysis the solid angle effect and nuclear deorientation also have to be taken into consideration [29, 30]. The solid angle effect plays a role at long target-to-degrader distances, when the solid angle is larger for the shifted than the degraded γ rays when the detectors are at backward angles. The nuclear spin alignment produced in the heavy ion induced fusion is perturbed when it recoils into vacuum. This leads to a time dependent angular dependence of the γ rays, which results as a difference between the observed intensity of the degraded and shifted components compared to the emitted intensities.

Other sources of inaccuracy are the relativistic effects on the solid angle arising from different recoil velocities and the detector efficiency because of different γ-ray energies [29, 30].

Chapter 5

Summary and outlook

The lifetime of the yrast 4^+ state in ^{182}Pt was determined with the RDDS method using 11 different target-to-degrader distances ranging from 3 µm to 4000 µm. The studied nuclei were produced in the ^{100}Mo(^{86}Kr, 4n)^{182}Pt fusion evaporation reaction. The velocity of the recoils was $0.0346(11)\,c$ after the target and $0.0255(11)\,c$ after the degrader. Recoil gated $\gamma\gamma$-matrices were analyzed with DDCM separately for each distance and the mean lifetime was calculated as the mean value from the obtained lifetimes.

The determined lifetime of the 4^+ state is 40.8(14) ps. From the lifetime the transition probability $B(E2)$ was calculated to be 221(8) W.u. Furthermore, this gives for the transition quadrupole moment $|Q_t| = 6.90(12)\,e$b, which corresponds to a deformation parameter $|\beta| = 0.243(4)$.

To draw any conclusions about collectivity of the prolate yrast states in ^{182}Pt, lifetimes for other yrast states have to be determined. From the data analyzed in this work it is possible to determine the lifetimes of yrast excited states up to the first 8^+ or 10^+ state, with the exception of the 2^+ state, which may have too long a lifetime to be obtained at the measured distances. Also the γ-ray energy might be too low to separate the shifted and degraded components.

After the systematics of the $|Q_t|$ of the prolate band in ^{182}Pt have been deciphered it will be possible to fully compare it to the neighboring nuclei. Before that, however, comparing the quadrupole moment of the 4^+ state to the other quadrupole moments of 4^+ states gives an idea of what can be expected. Quadrupole moments for 4^+ states in $N = 104$ isotones are presented in Fig. 5.1. The values have been normalized by dividing by Z to get rid of the charge dependence of the quadrupole moment. The quadrupole

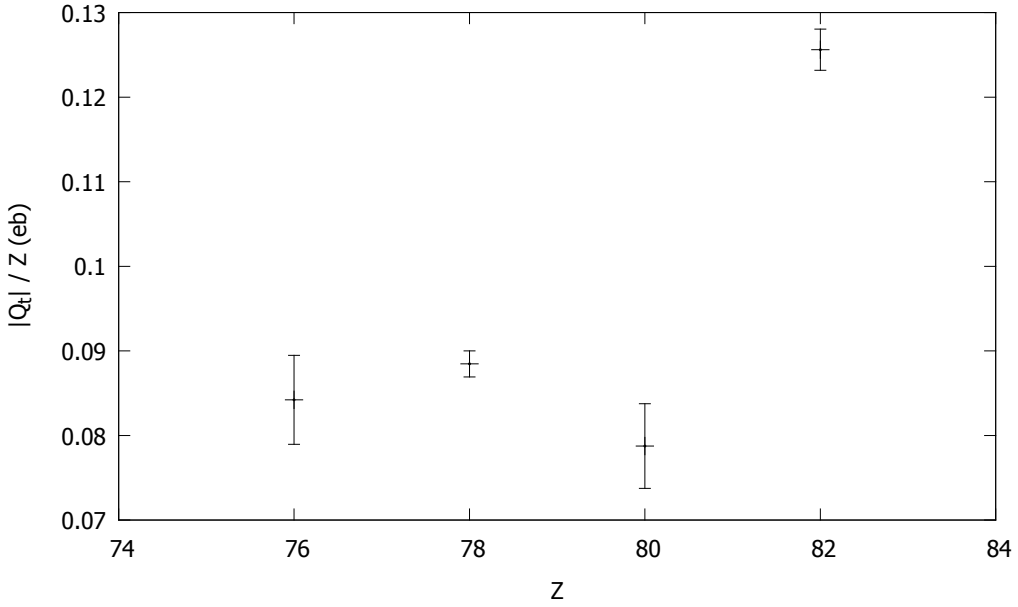

Figure 5.1. Quadrupole moments for the 4^+ states of ^{180}Os [31], ^{182}Pt, ^{184}Hg (lifetime from [10]) and ^{186}Pb [8]. The charge dependence of the quadrupole moment has been taken into account by dividing the values by Z.

moment of ^{186}Pb is significantly larger than the other quadrupole moments and it seems that the quadrupole moments decrease with decreasing proton number. The small quadrupole moment of ^{184}Hg can be explained with configuration mixing. The 4^+ state is a mixture of rotational and vibrational structures and thus has a significantly smaller quadrupole moment than the 6^+ state of ^{184}Hg. This can be seen in Fig. 2.3. One possible explanation for the decreasing quadrupole momnet is triaxiality. Before any further conclusions, lifetimes for other excited states in ^{182}Pt have to be analyzed.

Bibliography

[1] J. Suhonen, *From Nucleons to Nucleus* (Springer, 2007).

[2] R. F. Casten, *Nuclear Structure from a Simple Perspective* (Oxford University Press, 1990).

[3] A. Görgen, Journal of Physics G: Nuclear and Particle Physics **37**, 103101 (2010).

[4] K. S. Krane, *Introductory nuclear physics* (John Wiley & Sons, 1988).

[5] P. Rahkila, Ph.D. thesis, University of Jyväskylä (2010).

[6] C. D. Coster, B. Decroix, K. Heyde, J. L. Wood, J. Jolie, and H. Lehmann, Nuclear Physics A **621**, 802 (1997).

[7] J. Pakarinen, Ph.D. thesis, University of Jyväskylä (2005).

[8] T. Grahn, A. Dewald, O. Möller, R. Julin, C. W. Beausang, S. Christen, I. G. Darby, S. Eeckhaudt, P. T. Greenlees, A. Görgen, et al., Phys. Rev. Lett. **97**, 062501 (2006).

[9] T. Grahn, A. Petts, M. Scheck, P. A. Butler, A. Dewald, M. B. G. Hornillos, P. T. Greenlees, A. Görgen, K. Helariutta, J. Jolie, et al., Phys. Rev. C **80**, 014324 (2009).

[10] W. C. Ma, A. V. Ramayya, J. H. Hamilton, S. J. Robinson, J. D. Cole, E. F. Zganjar, E. H. Spejewski, R. Bengtsson, W. Nazarewicz, and J. Y. Zhang, Physics Letters B **167**, 277 (1986).

[11] D. Proetel, R. M. Diamond, and F. S. Stephens, Physics Letters B **48**, 102 (1974).

[12] U. Garg, A. Chaudhury, M. W. Drigert, E. G. Funk, J. W. Mihelich, D. C. Radford, H. Helppi, R. Holzmann, R. V. F. Janssens, T. L. Khoo, et al., Physics Letters B **180**, 319 (1986).

[13] T. Grahn, Ph.D. thesis, University of Jyväskylä (2006).

[14] W. Rother, Master's thesis, Institut für Kernphysik der Universität zu Köln (2008).

[15] A. Dewald, P. Sala, R. Wrzal, G. Böhm, D. Lieberz, G. Siems, R. Wirowski, K. O. Zeil, A. Gelberg, P. von Brentano, et al., Nuclear Physics A **545**, 822 (1992).

[16] C. W. Beausang, S. A. Forbes, P. Fallon, P. J. Nolan, P. J. Twin, J. N. Mo, J. C. Lisle, M. A. Bentley, J. Simpson, F. A. Beck, et al., Nuclear Instruments and Methods in Physics Research Section A: Accelerators, Spectrometers, Detectors and Associated Equipment **313**, 37 (1992).

[17] C. R. Alvarez, Nucl. Phys. News **3** (1993).

[18] G. Duchêne, F. A. Beck, P. J. Twin, G. de France, D. Curien, L. Han, C. W. Beausang, M. A. Bentley, P. J. Nolan, and J. Simpson, Nuclear Instruments and Methods in Physics Research Section A: Accelerators, Spectrometers, Detectors and Associated Equipment **432**, 90 (1999).

[19] M. Leino, J. Äystö, T. Enqvist, P. Heikkinen, A. Jokinen, M. Nurmia, A. Ostrowski, W. H. Trzaska, J. Uusitalo, K. Eskola, et al., Nuclear Instruments and Methods in Physics Research Section B: Beam Interactions with Materials and Atoms **99**, 653 (1995).

[20] R. D. Page, A. N. Andreyev, D. E. Appelbe, P. A. Butler, S. J. Freeman, P. T. Greenlees, R. D. Herzberg, D. G. Jenkins, G. D. Jones, P. Jones, et al., Nuclear Instruments and Methods in Physics Research Section B: Beam Interactions with Materials and Atoms **204**, 634 (2003).

[21] I. Lazarus, E. Appelbe, P. Butler, P. Coleman-Smith, J. Cresswell, S. Freeman, R. Herzberg, I. Hibbert, D. Joss, S. Letts, et al., Nuclear Science, IEEE Transactions on **48**, 567 (2001).

[22] E. S. Paul, P. J. Woods, T. Davinson, R. D. Page, P. J. Sellin, C. W. Beausang, R. M. Clark, R. A. Cunningham, S. A. Forbes, D. B. Fossan, et al., Phys. Rev. C **51**, 78 (1995).

[23] P. Rahkila, Nuclear Instruments and Methods in Physics Research Section A: Accelerators, Spectrometers, Detectors and Associated Equipment **595**, 637 (2008).

[24] *Evaluated nuclear structure data files (ensdf)*, `http://www.nndc.bnl.gov/ensdf/`.

[25] T. Grahn, A. Dewald, O. Möller, R. Julin, C. Beausang, S. Christen, I. Darby, S. Eeckhaudt, P. Greenlees, A. Görgen, et al., Nuclear Physics A **801**, 83 (2008), ISSN 0375-9474.

[26] A. Dewald, S. Harissopulos, and P. von Brentano, Zeitschrift für Physik A Hadrons and Nuclei **334**, 163 (1989).

[27] `http://www.ikp.uni-koeln.de/misc/doc/napa/napa.pdf`.

[28] T. Kibédi, T. Burrows, M. Trzhaskovskaya, P. Davidson, and C. N. Jr., Nuclear Instruments and Methods in Physics Research Section A: Accelerators, Spectrometers, Detectors and Associated Equipment **589**, 202 (2008).

[29] K. W. Jones, A. Z. Schwarzschild, E. K. Warburton, and D. B. Fossan, Phys. Rev. **178**, 1773 (1969).

[30] P. Petkov, S. Harissopulos, A. Dewald, M. Stolzenwald, G. Böhm, P. Sala, K. Schiffer, A. Gelberg, K. O. Zell, P. von Brentano, et al., Nuclear Physics A **543**, 589 (1992), ISSN 0375-9474.

[31] R. Kaczarowski, U. Garg, A. Chaudhury, E. G. Funk, J. W. Mihelich, D. Frekers, R. V. F. Janssens, and T. L. Khoo, Phys. Rev. C **41**, 2069 (1990).